SIMULATION OF ULTRAFAST FREE ELECTRON DYNAMICS AND TIME-DEPENDENT REFLECTIVITY IN SKIN-LIKE TISSUE MEDIA UNDER SHORTPULSE LASER EXCITATION

Submitted: 22.08.2025.

Accepted: 30.10.2025.

Esma Krvavac¹, Violeta Petrović¹, Hristina Delibašić Marković¹, Jelena Maljković²

¹University of Kragujevac, Faculty of Science, Radoja Domanovića 12, 34000 Kragujevac, Serbia, hristina.delibasic@pmf.kg.ac.rs

Coresponding author: Hristina Delibašić-Marković, University of Kragujevac, Faculty of Science, Radoja Domanovića 12, 34000 Kragujevac, Serbia, hristina.delibasic@pmf.kg.ac.rs

ABSTRACT

In this study, we investigate the ultrafast dynamics of free electrons in skin-like tissue media, stimulated by laser pulses with durations between 50 fs and 100 fs. Our analysis is based on a rate-equation approach for the evolution of free electron density $N_e(t)$ under different laser pulse durations. The simulated electron densities are then used to calculate the time-dependent change in reflectivity, $\Delta R(t)$, via a Drude-based dielectric function model and Fresnel equations for normal incidence. This enables us to assess the transient optical properties of tissue equivalents during and after ultrafast electronic excitation. The results highlight characteristic thresholds for carrier generation and show how pulse parameters influence the magnitude and temporal profile of $\Delta R(t)$. The presented approach offers a framework for understanding and predicting ultrafast reflectivity changes in tissue-like media, which can be useful for laser-based diagnostics, ultrafast imaging, and controlled photothermal treatments.

Keywords: free electron dynamics, skin-like tissue media.

INTRODUCTION

Ultrafast laser pulses have become an essential tool for exploring light-matter interactions in biological and tissue-like media. In the femtosecond to picosecond regime, this interaction is governed by nonlinear absorption mechanisms, including multiphoton ionization (MPI), tunneling ionization (TI), and subsequent avalanche ionization (AI), which lead to the rapid generation of free carriers before significant thermal or mechanical effects take place. Such processes occur on timescales much shorter than those of heat diffusion or stress wave propagation, enabling selective interaction with the target medium. This timescale separation enables high-precision material modification with minimal collateral damage, making ultrafast lasers valuable for biomedical imaging, microsurgery, and non-invasive diagnostics (Stuart et al., 1996; Vogel et al., 2005; Tirlapur and König, 2002). Understanding the underlying electron dynamics in these conditions provides the physical basis for interpreting time-resolved measurements and optimizing laser-based medical techniques.

Previous studies have developed both experimental and theoretical frameworks to characterize free carrier generation and its optical consequences. On the experimental side, time-resolved pump-probe reflectivity and transmission measurements have been used to analyze femtosecond-scale changes in refractive index and absorption, revealing distinct thresholds for carrier generation and transient reflectivity changes (Vogel et al., 2008; Krüger et al., 2020). These measurements not only map the ultrafast temporal evolution of the material response but also serve as basis for validating theoretical predictions. On the modeling side, rate-equation approaches have been widely adopted to describe the temporal evolution of free electron density $N_e(t)$, typically incorporating MPI and AI terms, as well as recombination processes (Rethfeld, 2004; Qiu et al., 2014). The flexibility of these models allows researchers to investigate a wide range of pulse durations, wavelengths, and fluences without requiring immediate experimental realization. These

²University of Belgrade, Institute of Physics Belgrade, Pregrevica 118, 11080 Belgrade, Serbia

models, coupled with dielectric function formalisms such as the Drude model, allow the computation of time-dependent optical properties, including the reflectivity change $\Delta R(t)$. In biological media such as skin, this approach has proven effective in linking microscopic electronic processes with macroscopic optical responses, providing a pathway toward quantitative interpretation of ultrafast laser-tissue interaction data.

In this work, we numerically investigate the ultrafast generation and evolution of free electrons in skin-like tissue equivalents excited by laser pulses of durations between 50 fs and 100 fs ($1fs = 1 \times 10^{-15}s$). We use a rate-equation model to calculate $N_e(t)$ for different pulse durations and then determine $\Delta R(t)$ using a Drude-based dielectric function in combination with Fresnel equations at normal incidence. By systematically varying the excitation parameters, we identify correlations between the laser pulse characteristics and the temporal evolution of the transient optical response. This allows us to identify characteristic thresholds for carrier generation and to examine how laser pulse duration influences both the magnitude and temporal evolution of the transient reflectivity signal. The developed approach provides insight into the correlation between excitation conditions and the resulting ultrafast optical response of tissue-like media.

The remainder of this paper is organized as follows. Section 2 describes the theoretical framework, including the rate-equation model for free electron generation and the optical model used for calculating transient reflectivity. Section 3 reports and discusses simulation results, focusing on the dependence of $N_e(t)$ and $\Delta R(t)$ on pulse duration, fluence, and wavelength. Section 4 summarizes the key findings presented in this study.

THEORETICAL FRAMEWORK

When an ultrashort laser pulse impinges on a skin-like tissue model, the very first physical consequence is the rapid generation of free carriers within the material. This process take place on a sub-picosecond timescale, well before any significant heat conduction or mechanical stress relaxation can occur. At such ultrafast temporal scales, electronic excitation dynamics dominate over thermal or structural changes. The primary mechanisms responsible for the formation of conduction-band electrons are photoionization and AI. These processes act in concert to determine the instantaneous free-electron density $N_e(t)$, a quantity that critically influences the optical response of the medium during and after the laser–matter interaction (Couairon and Mysyrowicz, 2007; Stuart et al., 1996). For this purpose, the skin-like tissue medium is modelled using optical and electronic parameters representative of hydrated biological and water-based materials, as reported in (Vogel et al. (2005), Qiu et al. (2014), and Krüger et al. (2020)).

The initiation of ionization is governed by photoionization, which in general may proceed via MPI or TI. Under the irradiation conditions considered here (near-infrared femtosecond pulses at moderate intensities) the interaction is well described within the multiphoton picture, and TI contributions can be neglected. In the MPI regime, a bound electron simultaneously absorbs an integer number K of photons, such that the total absorbed photon energy exceeds not only the material's bandgap E_g , but also the ponderomotive potential U_p , which represents the cycleaveraged quiver energy of a free electron in the laser field. The smallest such integer is:

$$K = \langle \frac{E_g + U_p}{\hbar \omega} \rangle \tag{1}$$

where ω is the laser angular frequency. The ponderomotive potential is given by:

$$U_p = \frac{e^2 E^2}{4m\omega^2} _{or} U_p[eV] \approx 9.33 \times 10^{-14} I[W/cm^2] \lambda^2 [\mu m^2]$$
 (2)

and represents the cycle-averaged quiver energy of a free electron in the oscillating electric field of the laser. It depends on the elementary charge e, the electron rest mass m, the peak electric field

amplitude E, the instantaneous laser intensity I, and the laser wavelength λ . Physically, U_p increases with both the laser intensity and the square of the wavelength, reflecting the stronger and slower oscillations experienced by the electron in such conditions. At sufficiently high intensities, the effective ionization threshold becomes $E_g + U_p$, meaning that the electron must absorb enough photon energy to overcome not only the material bandgap E_g but also the additional energy associated with its oscillatory motion in the field. However, for moderate intensities where $U_p \ll E_g$, the ponderomotive contribution is negligible, and the minimum number of photons required for MPI reduces to $K = \langle E_g / \hbar \omega \rangle$.

Since the ponderomotive term, U_p , can effectively raise the ionization threshold, the overall probability of MPI is linked to the instantaneous laser intensity. This naturally leads to a description of the process in terms of an intensity-dependent ionization rate. The efficiency of MPI is strongly intensity-dependent and can be described by a power-law rate:

$$W_{MPI}(I) = \sigma_K I^K \qquad (3)$$

Here, σ_K is the generalized K-photon absorption cross-section, a material-specific constant typically determined experimentally or from nonlinear optical theory (Reiss, 1992; Smith and Gallagher, 1988). Its value can vary by orders of magnitude depending on the material's structure, photon energy, and configuration (Couairon and Mysyrowicz, 2007; Denk et al., 1995; Delone and Krainov, 2000). In particular, multiphoton microscopy literature provides quantitative measurements of multiphoton cross-sections in biological tissues and fluorescing media, which helps anchor plausible values for tissue-like materials in modeling studies (Denk et al., 1995; Couairon and Mysyrowicz, 2007).

Once a seed population of conduction-band electrons is generated through MPI, further carrier multiplication can occur via AI. In this process, the existing free electrons absorb additional energy from the laser field between successive collisions with the lattice. If the acquired kinetic energy exceeds the impact-ionization threshold, typically close to the bandgap energy, these electrons can liberate additional bound electrons, initiating a collisional cascade. As a result, the free-electron density grows nonlinearly during the pulse, often leading to a rapid transition from a weakly ionized to a strongly ionized state. The avalanche growth rate is commonly modelled as:

$$W_{AI}(I, N_e) = \alpha(I)IN_e \tag{4}$$

where α is the avalanche coefficient, determined by the electron–phonon scattering rate, the mean free path, and the threshold energy for impact ionization (Stuart et al., 1996; Rethfeld et al., 2004). In the present simulations, α was modeled as an intensity-dependent parameter, reflecting the fact that the efficiency of impact ionization increases with the instantaneous laser field strength. The dependence was expressed as: $\alpha(I) = \alpha_0/I$, with $\alpha_0 = 5 \times 10^{10} \ s^{-1}$. This is in accordance with reported values for skin-like tissue analogues (Rethfeld et al., 2004; Vogel et al., 2005). Such formulation provides a realistic scaling of the avalanche rate under femtosecond excitation and couples to the seed population generated by MPI, meaning that without the initial multiphoton-generated carriers, AI would not be initiated under the present irradiation conditions.

Once the seed electron population has been generated by MPI and subsequently amplified through AI, the time evolution of the free-electron density is governed by a competition between generation and loss mechanisms. While MPI acts as an ultrafast source term active primarily during the laser pulse, AI can continue to operate throughout the pulse duration, leading to exponential carrier

multiplication. Simultaneously, recombination processes act to reduce the electron density once electrons are promoted to the conduction band. The interplay of these contributions can be expressed through the rate equation for the electron density:

$$\frac{dN_e}{dt} = W_{MPI}(I) + W_{AI}(I, N_e) - \frac{N_e}{\tau_r}$$
 (5)

Here, the first term represents photoionization-induced seeding, the second term accounts for avalanche growth, and the last term describes electron recombination with an effective lifetime τ_r . This term incorporates both radiative and nonradiative recombination channels, and in biological or skin-like media it can range from a few to hundreds of picoseconds, depending on microscopic structure, defect density, and impurity levels (Vogel et al., 2005).

Since the laser pulse has a finite temporal envelope, the instantaneous intensity I(t) must be explicitly accounted for in all rate expressions. For a transform-limited Gaussian pulse with full width at half maximum (FWHM) duration $^{\tau}p$ and peak intensity I_0 , the temporal profile is given by:

$$I(t) = I_0 exp[-4ln2(\frac{t}{\tau_p})^2]$$
(6)

This functional form ensures that I(t) correctly describes the rise and decay of the pulse around its temporal center. Because both MPI and AI rates scale with the instantaneous intensity, the temporal envelope directly governs the growth dynamics of $N_e(t)$ in simulations. In particular, for femtosecond-scale pulses, the sharp temporal localization of I(t) means that most of the free-electron population is generated within only a few optical cycles near the peak of the pulse.

The temporal evolution of $N_e(t)$, governed by the coupled MPI and AI processes under the finite pulse envelope, is not just a theoretical framework. It directly determines how the material's optical properties change during and after the laser-matter interaction. In particular, the accumulation of free carriers alters the dielectric response of the medium on femtosecond timescales, leading to measurable changes in its reflectivity and transmission. To capture this effect quantitatively, we describe the optical response using the Drude free-electron model (Sokolowski-Tinten and von der Linde, 2000; Rethfeld et al., 2004):

$$\varepsilon(\omega,t) = \varepsilon_b(\omega) - \frac{N_e(t)e^2}{\varepsilon_0 m^*} \bullet \frac{1}{\omega^2 + i\gamma\omega}$$
 (7)

where $\varepsilon_b(\omega)$ is the unperturbed dielectric constant, m^* is the effective electron mass, and γ is the electron collision frequency. At normal incidence, the reflectivity follows from the Fresnel formula:

$$R(t) = \left| \frac{\sqrt{\varepsilon(\omega, t)} - 1}{\sqrt{\varepsilon(\omega, t)} + 1} \right|^2 \tag{8}$$

The transient reflectivity change, a key observable in pump-probe experiments, is defined as (Sundaram and Mazur, 2002; Vogel et al., 2005):

$$\Delta R(t) = R(t) - R_0 \qquad (9)$$

where R_0 denotes the reflectivity in the absence of the pump pulse. This quantity encodes the ultrafast dynamics of free-electron generation and decay, allowing direct comparison between simulations and experimental measurements. By coupling the ionization rate equations with the Drude optical model, we establish a predictive framework that links laser parameters (pulse duration and wavelength) to measurable optical signatures such as $\Delta R(t)$. This integrated approach forms the basis of our numerical simulations presented in the next section.

RESULTS AND DISSCUSION

In this section, we present numerical simulations of ultrafast free-carrier generation and its impact on the transient optical response of a skin-like medium under laser excitation. The results are obtained by solving the rate equations for MPI, AI, and carrier recombination (see Eq. (4)), using the Gaussian temporal envelope (Eq. (5)) of the incident laser pulse as described in the theoretical framework. The simulations are designed to reveal the interplay between the initial seeding of conduction-band electrons through MPI, their subsequent multiplication via AI, and their decay through recombination channels. By tracking the full temporal evolution of the free-electron density $N_e(t)$ for different pulse durations, we can identify the dominant processes governing carrier dynamics on sub-picosecond timescales. These carrier populations are then coupled to the Drude optical model to calculate the transient reflectivity change $\Delta R(t)$, which serves as a direct observable for comparison with ultrafast pump-probe experiments (Vogel et al., 2005; Stuart et al., 1996; Rethfeld et al., 2004; Sundaram and Mazur, 2002).

Fig. 1 presents the simulated temporal evolution of the free-electron density in a skin-like medium for two different femtosecond pulse durations: 50 fs and 100 fs, at identical peak intensity $I_0 = 1 \times 10^{14} W/cm^2$. The simulation shown here corresponds to the MPI-only regime, where AI and recombination are initially neglected in order to isolate the seeding stage of free-carrier generation.

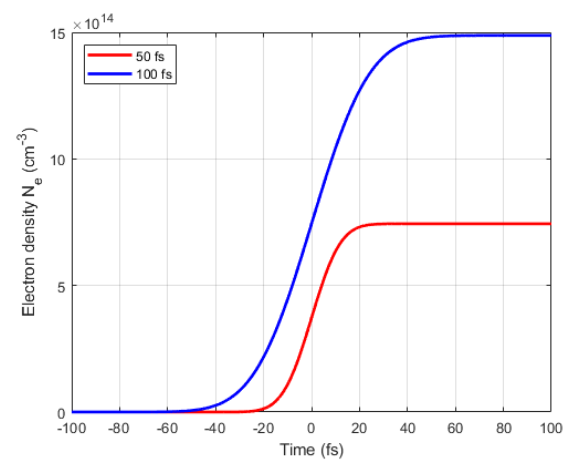


Figure 1. Temporal evolution of the free-electron density $N_e(t)$ in a skin-like medium for Gaussian laser pulses with durations of 50 fs (red) and 100 fs (blue) at the same peak intensity, $I_0=1\times 10^{14}W/cm^2$ including MPI.

The growth of $N_e(t)$ in Fig. 1 follows the temporal structure of the laser intensity envelope, but the magnitude of the final densities is dictated by how long the material remains under conditions favorable for MPI. Multiphoton ionization is a high-order non-linear process in which the instantaneous ionization rate depends steeply on the laser intensity, I, scaling as $W_{MPI} \propto I^K$,

where K is the number of photons required to cross the bandgap. This dependence means that significant ionization occurs only in the central part of the pulse where I(t) approaches its maximum. For the shorter, 50-fs pulse, the high-intensity window is extremely narrow. The field amplitude rises and falls rapidly, and although the instantaneous rate W_{MPI} reaches the same peak value as in the 100-fs case, the available time for sustained ionization is short. As a result, the integrated number of photon-absorption events per atom is smaller, and the final free-electron density is correspondingly reduced. For the 100-fs pulse, the broader temporal envelope keeps the intensity above the multiphoton threshold for roughly twice as long, effectively increasing the "interaction time" during which MPI can proceed efficiently. This difference directly translates into a greater cumulative electron yield. Quantitatively, the final simulated values are: $N_{e,final}^{50fs} \approx 7.44 \times 10^{14} cm^{-3}$ and $N_{e,final}^{100fs} \approx 1.49 \times 10^{15} cm^{-3}$. These values are consistent with literature reports for pure MPI in water and biological-tissue analogues, where carrier densities on the order of $10^{14} - 10^{15} cm^{-3}$ are typically observed before AI becomes significant (Vogel et al., 2005; Stuart et al., 1996; Rethfeld et al., 2004). The temporal profiles themselves carry important physical signatures. In the pre-pulse wings (t < -20 fs for the 50-fs case, t < -40 fs for the 100-fs case), the laser intensity is too low to drive noticeable MPI, so $N_e(t)$ stays essentially at zero. As the pulse approaches its peak, the steep I^K dependence causes a rapid, exponential rise in $N_e(t)$, visible as the sharp up-turn in the semilogarithmic plot. The rise is slightly more gradual in the 100-fs case because the intensity ramp-up is slower, but the integrated area under the rate curve is significantly larger. After the pulse maximum, I(t) decays symmetrically, the MPI rate drops sharply, and the curves flatten into a saturation plateau. The plateau value corresponds to the total density of seed electrons generated by MPI over the entire pulse. These MPI-generated seed populations form the initial condition for AI in realistic breakdown scenarios. In practice, once AI becomes active, the carrier density can grow by several orders of magnitude within only a few femtoseconds after the peak, but the efficiency of AI depends strongly on the seed density produced by MPI. Thus, differences in pulse duration, even at constant peak intensity, can have a decisive impact on the onset and progression of optical breakdown, as observed in (Stuart et al., 1996; Rethfeld et al., 2004; Vogel et al., 2005; Couairon and Mysyrowicz, 2007).

Following the MPI-only results in Fig. 1, Fig. 2 shows the simulated free electron density evolution when MPI, AI, and carrier recombination are all considered. In this regime, the MPI-generated seed electrons are rapidly multiplied through AI, where existing free carriers gain energy from the laser field via inverse Bremsstrahlung absorption and subsequently create secondary electron-hole pairs by impact ionization (Rethfeld et al., 2004; Stuart et al., 1996; Vogel et al., 2005). Since the AI rate is proportional to both the instantaneous laser intensity and the current carrier density, its contribution grows explosively once a sufficient seed population is present. This multiplicative process strongly depends on how long the optical field remains above the AI activation threshold, making the pulse duration a decisive parameter. In addition to these ionization channels, carrier recombination acts as a concurrent loss mechanism, whereby free electrons and holes annihilate over a characteristic recombination time. This process counteracts the increase of $N_e(t)$ and becomes particularly significant once the laser intensity has dropped below the AI threshold, limiting the persistence of high carrier densities after the pulse maximum. The balance between avalanche growth and recombination thus shapes not only the peak values but also the post-peak decay rate of $N_e(t)$.

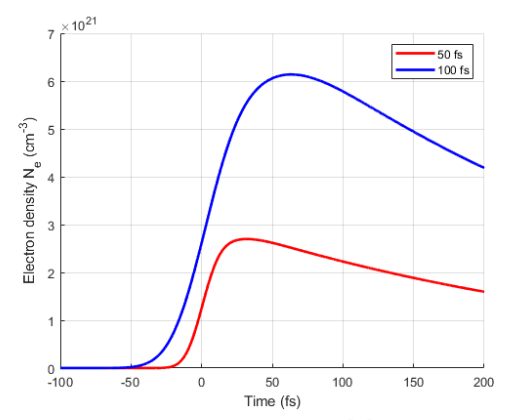
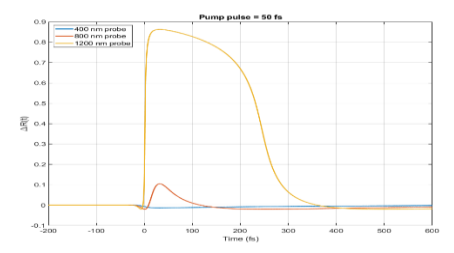


Figure 2. Temporal evolution of the free-electron density $N_e(t)$ in a skin-like medium for Gaussian laser pulses with durations of 50 fs (red) and 100 fs (blue) at the same peak

intensity, $I_0 = 1 \times 10^{14} W/cm^2$ including MPI, AI and carrier recombination.

Both curves presented in Fig. 2 share the same initial phase: during the rising edge of the pulse, MPI seeds a small population of conduction-band electrons. As soon as this seed density becomes sufficient, AI sets in and drives a rapid increase in $N_e(t)$. The avalanche growth rate depends simultaneously on the field strength and the number of carriers already present, creating a positive feedback loop. The effect of pulse duration on this growth is evident. In the 50-fs case, the high-intensity window is narrow, and the AI phase is comparatively short-lived. The electron density rises saturates reaching steeply but earlier, critical $_{e,critical}^{50fs} \approx 2.698 \times 10^{21} cm^{-3}$ at $t \approx 32fs$, after which recombination drives a gradual decay. For the 100-fs pulse, the broader envelope sustains strong AI for nearly twice as long. This extended interaction time allows the carrier density to grow well beyond the critical plasma density for 800 nm light, peaking at $N_{e,critical}^{100fs} \approx 6.139 \times 10^{21} cm^{-3}$ at $t \approx 63 fs$, before recombination begins to dominate the decay phase. The absolute values and timing of the peaks are physically consistent with ultrafast breakdown dynamics reported in the literature (e.g., Stuart et al., 1996; Rethfeld et al., 2004; Vogel et al., 2005). The later and higher peak in the longer pulse case reflects the fact that avalanche multiplication continues well into the trailing edge of the pulse, while the faster decay in the shorter pulse case highlights the stronger relative influence of recombination once AI ceases. These trends are quantitatively and qualitatively consistent with ultrafast breakdown dynamics observed in water and tissue analogues, where avalanche growth dominates the early evolution and recombination governs the relaxation phase (Stuart et al., 1996; Rethfeld et al., 2004; Vogel et al., 2005; Bulgakova & Rethfeld, 2010).

Following the carrier-density dynamics presented in Fig. 2, the simulated temporal profiles of $N_e(t)$ are coupled to the Drude model to calculate the time-resolved reflectivity change $\Delta R(t)$ for three probe wavelengths: 400 nm, 800 nm, and 1200 nm. This step provides a direct link between the ultrafast ionization physics and an experimentally accessible observable in femtosecond pump-probe reflectometry. Fig. 3 shows the resulting $\Delta R(t)$ traces for Gaussian pump pulses of 50 fs and 100 fs duration at the same peak intensity $I_0 = 1 \times 10^{14} W/cm^2$ as before. The spectral dependence of the probe response emerges naturally from the Drude formalism, where the transient plasma frequency depends on $N_e(t)$ and competes with the probe frequency in determining the complex refractive index and reflectivity (Vogel et al., 2005; García-Lechuga et al., 2017; Bonse et al., 2020; Inogamov et al., 2020).



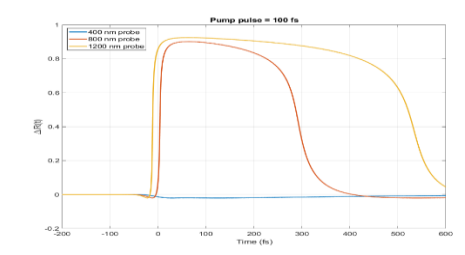


Figure 3. Simulated transient reflectivity change $\Delta R(t)$ for Gaussian pump pulses of 50 fs and 100 fs duration at $I_0 = 1 \times 10^{14} W/cm^2$, probed at 400 nm (blue), 800 nm (red), and 1200 nm (yellow). The model includes MPI, AI, and carrier recombination.

For both pulse durations, the evolution of $\Delta R(t)$ reflects the steep onset of AI once the MPI-generated seed density surpasses the critical level required for efficient carrier multiplication. The probe wavelength strongly influences the magnitude of the transient reflectivity change. At 400 nm, the probe frequency is much higher than the transient plasma frequency throughout the interaction, so the refractive index perturbation is weak and $\Delta R(t)$ remains essentially zero in both cases. At 800 nm, the situation changes dramatically once $N_e(t)$ approaches the corresponding critical plasma density; here, the real part of the refractive index drops sharply, and $\Delta R(t)$ rises to pronounced peaks, reaching values close to unity for the 100-fs pulse. At 1200 nm, the high free-carrier densities reached during the excitation significantly enhance the refractive index contrast with the surrounding medium, producing strong positive reflectivity changes for both pulse durations. These wavelength-dependent trends are consistent with ultrafast optical breakdown studies in biological-tissue analogues (Stuart et al., 1996; Rethfeld et al., 2004; Golik et al., 2015; Bonse et al., 2020; Inogamov et al., 2020). The influence of pulse duration on $\Delta R(t)$ is equally evident. In the 50-fs case, the high-intensity portion of the pump envelope is short-lived, limiting the time available for avalanche multiplication. The reflectivity therefore rises steeply but reaches a lower maximum before recombination starts to dominate, and it decays more rapidly once the pump has passed. In contrast, the 100-fs pulse maintains its intensity above the avalanche threshold for nearly twice as long, allowing $N_e(t)$ to exceed the critical plasma density for both 800 nm and 1200 nm probes by a substantial margin. As a result, $\Delta R(t)$ not only reaches higher values but also remains elevated for a longer duration before the onset of recombination-driven decay. The temporal asymmetry in all curves reflects the delayed onset of avalanche growth relative to the pulse maximum and the persistence of recombination after the pump field has vanished. Such behaviour has been observed experimentally in femtosecond pumpprobe studies of water, polymers, and skin-like phantoms (Golik et al., 2015; Mareev et al., 2024), confirming that the interplay of seeding, multiplication, and loss governs both the magnitude and the temporal profile of the transient reflectivity signal. It is important to state that this quantitative correspondence is further supported by the fact that the simulated peak reflectivity changes $(\Delta R \approx 0.8 - 0.9 \text{ at } 800 - 1200nm)$ and corresponding critical plasma densities ($\sim 10^{21} cm^{-3}$) closely match experimentally reported values presented in (Vogel et al., 2005; Golik et al., 2015; Mareev et al., 2024). These consistencies confirm that the chosen parameters and rate-equation model reproduce experimentally observed magnitudes and timescales of ultrafast reflectivity dynamics.

To further quantify the spectral dependence of the transient reflectivity response, we extracted the maximum values of $\Delta R(t)$ from the full pump-probe traces at each probe wavelength. This analysis enables a direct comparison between the short-pulse (50 fs) and long-pulse (100 fs) excitation regimes, highlighting how the interplay between MPI, AI, and recombination manifests across the near-infrared and visible spectrum.

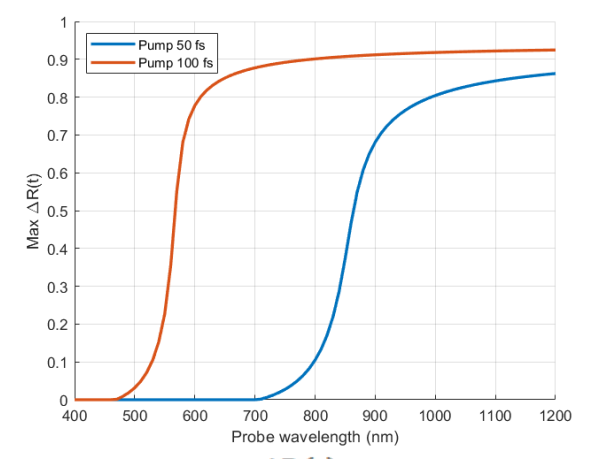


Figure 4. Maximum transient reflectivity change, $\Delta R(t)$, as a function of probe wavelength for 50 fs (blue) and 100 fs (orange) pump pulses at peak intensity ($I_0 = 1 \times 10^{14} W/cm^2$) in a skin-like medium. Values correspond to the peak of the $\Delta R(t)$ traces shown in Fig. 3.

The spectral dependence of the peak reflectivity change exhibits a pronounced sigmoidal transition from near-zero response at shorter probe wavelengths to large positive values in the near-infrared. For the 50-fs pump pulse, this transition occurs gradually, negligible $\Delta R(t)$ below ~750 nm and a steep increase between 800 nm and 1000 nm, eventually reaching saturation at ~0.85 around 1200 nm. In contrast, the 100-fs pulse produces a significantly earlier onset of the high- $\Delta R(t)$ regime, with a sharp rise already evident near 600-650 nm and saturation close to 0.9 for longer wavelengths. Physically, this shift reflects the higher free-carrier densities generated under the longer pulse excitation, which increase the refractive index contrast and modify the complex dielectric function more strongly across a broader spectral range (Rethfeld et al., 2004; Vogel et al., 2005; García-Lechuga et al., 2017; Inogamov et al., 2020). The earlier spectral onset for the 100-fs pulse is consistent with the fact that AI is sustained for a longer fraction of the pulse envelope, leading to higher peak carrier densities and thus stronger perturbations to the optical response. At the shortest probe wavelengths (< 600 nm), the reflectivity change remains minimal for both pulse durations because the Drude-like carrier contribution is small compared to the background response dominated by bound-electron absorption. In contrast, at longer wavelengths (> 800 nm), the free-carrier contribution becomes dominant, resulting in strong positive $\Delta R(t)$. For the 100-fs case, this regime extends well into the visible, while for the 50-fs case, it is confined primarily to the near-infrared. This difference clearly illustrates how pulse duration governs not only the temporal evolution of the transient optical signal but also its spectral distribution, a fact with direct implications for pump-probe measurements on biological tissue analogues.

Finally, examining how the maximum reflectivity changes maximum value of $\Delta R(t)$ varies with pulse duration τ_p offers direct insight into the onset and saturation of laser-induced plasma formation across different wavelengths. This analysis captures the combined effects of MPI, AI, and carrier recombination under identical peak intensities as in Figs. 1-4.

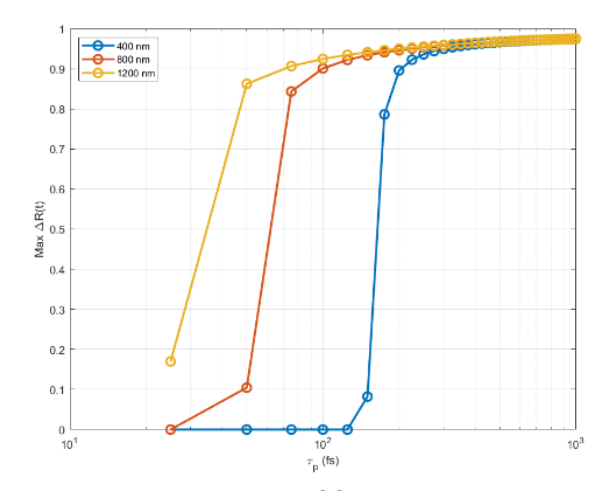


Figure 5. Maximum relative reflectivity changes $\Delta R(t)$ as a function of laser pulse duration τ_p for three wavelengths: 400 nm (blue), 800 nm (red), and 1200 nm (yellow). The peak intensity is kept constant across all cases.

The curves in Fig. 5 reveal a pronounced threshold-like behavior in maximal value $\Delta R(t)$ with respect to τ_p , reflecting the cumulative action of MPI and AI in generating a dense free-electron plasma. At 1200 nm, the threshold occurs for the shortest pulses among the three wavelengths. This is attributed to the relatively low MPI order and larger penetration depth at longer wavelengths, which facilitates faster carrier accumulation. At 800 nm, the threshold shifts to longer pulses, consistent with a higher MPI order and reduced penetration depth. For 400 nm, the threshold is reached only for significantly longer pulses, indicating that high-order MPI dominates the seeding process and requires extended exposure above the AI activation threshold for efficient plasma growth. In all cases presented in Fig. 5, once the threshold is surpassed, maximal value of $\Delta R(t)$ rapidly approaches unity, signifying near-complete plasma screening of the incident light. The saturation regime indicates that further increases in τ_p do not produce substantial additional reflectivity changes, as the electron density already exceeds the critical density for the given wavelength.

CONCLUSIONS

The numerical results presented in this study show that the spectral and temporal characteristics of the transient reflectivity in skin-like media are governed by the coupled dynamics of multiphoton seeding, avalanche multiplication, and carrier recombination. Longer pump pulses extend the temporal window above the AI threshold, enabling higher peak carrier densities that exceed the critical plasma density for a wider range of probe wavelengths. This enhanced free-carrier population increases the refractive index perturbation predicted by the Drude model, shifting the onset of strong positive ΔR toward shorter wavelengths and broadening the spectral domain of pronounced response. In contrast, shorter pulses limit avalanche growth, leading to lower $N_e(t)$ peaks, faster recombination-driven decay, and a delayed spectral onset of high reflectivity. These findings highlight the decisive role of pulse-duration-controlled carrier kinetics in shaping both the magnitude and spectral distribution of ultrafast optical signatures in tissue-like media.

Beyond their theoretical relevance, the results presented in this study also outline the physical limits within which femtosecond irradiation can be precisely controlled. The established

correlation between excitation parameters and transient reflectivity thus provides a quantitative framework that may guide future applications in ultrafast laser diagnostics and selective photothermal interaction regimes.

ACKNOWLEDMENTS

Authors would like to acknowledge the support received from the Science Fund of the Republic of Serbia, #GRANT 6821, Atoms and (bio) molecules-dynamics and collisional processes on short time scale - ATMOLCOL. Our appreciation also goes to the Serbian Ministry of Education, Science and Technological Development (Agreement No. 451-03-136/2025-03/200122). H. Delibašić Marković would also like to express gratitude to COST Actions CA21159 - "Understanding interaction of light with biological surfaces: possibility for new electronic materials and devices" for their support.

DECLARATIONS OF INTEREST STATEMENT

The authors affirm that there are no conflicts of interest to declare in relation to the research presented in this paper

LITERATURE

- Bonse, J., Kirner, S.V. and Krüger, J. (2020). Laser-induced periodic surface structures (LIPSS). *Handbook of laser micro-and nano-engineering*, 1-59.
- Carrasco-García, I., Vadillo, J.M. and Laserna, J.J. (2015). Visualization of surface transformations during laser ablation of solids by femtosecond pump—probe time-resolved microscopy. *Spectrochimica Acta Part B: Atomic Spectroscopy*, 113, 30-36.
- Couairon, A., and Mysyrowicz, A. (2007). Femtosecond filamentation in transparent media. *Physics Reports*, 441(2–4), 47–189.
- Delone, N. B., and Krainov, V. P. (2000). Multiphoton processes in atoms. Springer.
- Denk, W., Strickler, J. H., and Webb, W. W. (1990). Two-photon laser scanning fluorescence microscopy. *Science*, 248(4951), 73–76.
- García-Lechuga, M., Haahr-Lillevang, L., Siegel, J., Balling, P., Guizard, S. and Solis, J. (2017). Simultaneous time-space resolved reflectivity and interferometric measurements of dielectrics excited with femtosecond laser pulses. *Physical Review B*, *95*(21), 214114.
- Golik, S.S., Ilyin, A.A., Babiy, M.Y., Biryukova, Y.S., Lisitsa, V.V. and Bukin, O.A. (2015). Determination of iron in water solution by time-resolved femtosecond laser-induced breakdown spectroscopy. *Plasma Science and Technology*, 17(11), 975.
- Inogamov, N.A., Petrov, Y.V., Khokhlov, V.A. and Zhakhovskii, V.V. (2020). Laser ablation: physical concepts and applications. *High Temperature*, 58(4), 632-646.
- Krüger, J., Wang, J., Kautek, W. (2020). Ultrafast laser processing of transparent materials. *Appl. Surf. Sci.*, 506, 144998.
- Mareev, E.I., Asharchuk, N.M., Rovenko, V.V. and Yusupov, V.I. (2024). Dynamics of Water Transition to the Supercritical State under Ultrafast Heating with Ultrashort Laser Pulses. *Russian Journal of Physical Chemistry B*, 18(8), 1905-1915.
- Qiu, J., Jia, W., Lin, C., Hirao, K. (2014). Ultrafast free carrier dynamics in dielectrics. *Opt. Express*, 22(19), 23374-23381.
- Rethfeld, B. (2004). Unified model for the free-electron avalanche in laser-irradiated dielectrics. *Phys. Rev. Lett.*, 92(18), 187401.
- Rethfeld, B., Sokolowski-Tinten, K., von der Linde, D., and Anisimov, S. I. (2004). Timescales in the response of materials to femtosecond laser excitation. *Applied Physics A*, 79, 767–769.
- Sokolowski-Tinten, K., and von der Linde, D. (2000). Generation of dense electron–hole plasmas in silicon. *Physical Review B*, 61(4), 2643–2650.
- Stuart, B. C., Feit, M. D., Herman, S., Rubenchik, A. M., Shore, B. W., and Perry, M. D. (1996). Optical ablation by high-power short-pulse lasers. *Journal of the Optical Society of America B*, 13(2), 459–468.

- Delibašić-Marković, H., et al. (2025). Simulation of ultafast free electron dynamics and time-dependent reflectivity skin-like tissue media under shortpuls laser excitation. *STED Conference* 14(2), 515-526.
- Tirlapur, U., König, K. (2002). Targeted transfection by femtosecond laser. *Nature*, 418(6895), 290-291.
- Vogel, A., Linz, N., Freidank, S., Paltauf, G. (2008). Femtosecond-laser-induced nanocavitation in water: Implications for optical breakdown threshold and cell surgery. *Phys. Rev. Lett.*, 100(3), 038102.
- Vogel, A., Noack, J., Hüttman, G., Paltauf, G. (2005). Mechanisms of femtosecond laser nanosurgery of cells and tissues. *Appl. Phys. B*, 81(8), 1015-1047.